Journal of Materials Chemistry A

ROYAL SOCIETY OF CHEMISTRY

PAPER

View Article Online
View Journal

Check for updates

Cite this: DOI: 10.1039/d4ta01608d

Ultrathin NiO nanosheets anchored to a nitrogen-doped dodecahedral carbon framework for aqueous potassium-ion hybrid capacitors†

Tianlu Wang,‡[a] Wei Zong,‡[a] Jieru Yang,‡[a] Leiqian Zhang,[a] Jian Meng,[a] Jiale Ge,[a] Guozheng Yang,[b] Jianguo Ren,[c] Peng He,[c] Elke Debroye,[d] Jean-François Gohy,[e] Tianxi Liu*[a] and Feili Lai*[bd]

Received 9th March 2024
Accepted 18th June 2024

DOI: 10.1039/d4ta01608d

rsc.li/materials-a

Hierarchical porous structures and well-modulated interfacial interactions are essential for the performance of electrode materials. The energy storage performance can be promoted by regulating the diffusion behavior of the electrolyte and constructing a coupled interaction at heterogeneous interfaces. Herein, we have synthesized ultrathin NiO nanosheets anchored to nitrogen-doped hierarchical porous carbon (NiO/N-HPC) and applied it to construct aqueous potassium ion hybrid capacitors (APIHCs). The abundant and interconnected porous architecture promotes electrolyte penetration/diffusion and shortens the ion transport path, thereby accelerating storage reaction kinetics. The nitrogen-doped carbon support can achieve optimized metal oxides–carbon interaction and enhance the adsorption ability for the electrolyte ions, leading to earning higher storage capacity. Consequently, the prepared NiO/N-HPC exhibits a superior capacitance of 126.4 F g^{-1} at a current density of 0.5 A g^{-1}, and the as-fabricated NiO/N-HPC//N-HPC APIHC achieves an ultra-high capacitance retention of 91.6% over 8000 cycles at a current density of 2 A g^{-1}. Meanwhile, the APIHC device shows an excellent energy density of 21.95 W h kg^{-1} and a power density of 9000 W kg^{-1}.

Feili Lai

Dr Feili Lai obtained his master's degree (2017) and PhD degree (2019) from Fudan University and Max Planck Institute of Colloids and Interfaces/Universität Potsdam, respectively. He worked as Postdoc Research Fellow at KU Leuven, and as Visiting Scholars at Max Planck Institute for Polymer Research and Harvard University. He is currently an Associate Professor at Shanghai Jiao Tong University, and his research interests combine the design and synthesis of low-dimensional solids for energy storage and conversion applications, as well as the 4D soft robotics.

1 Introduction

The growing demands for electric vehicles and massive smart grids have been driving advances in energy storage devices with high power and energy densities.[1–3] Among multitudinous energy storage systems, rechargeable metal-ion batteries (RIBs) and supercapacitors (SCs) represent promising ones that can advance both research and practical applications.[4–8] However, the unsatisfactory power density of RIBs and low energy density of SCs make them challenging to meet the future needs for simultaneous high energy density and output power, known as the Ragone conflict. Lithium-ion hybrid capacitors (LIHCs) provide a potential solution by combining the benefits of SCs and RIBs to strike a balance between high power and energy densities while maintaining a long lifetime.[9–11] Nevertheless, the development of LIHCs is constrained by the uneven distribution of lithium resources and rising costs. Aqueous potassium-ion hybrid capacitors (APIHCs) have emerged as an

[a]Key Laboratory of Synthetic and Biological Colloids, Ministry of Education, School of Chemical and Material Engineering, International Joint Research Laboratory for Nano Energy Composites, Jiangnan University, Wuxi, 214122, P. R. China. E-mail: txliu@jiangnan.edu.cn

[b]State Key Laboratory of Metal Matrix Composites, School of Materials Science and Engineering, Shanghai Jiao Tong University, Shanghai, 200240, P. R. China. E-mail: feililai@sjtu.edu.cn

[c]BTR New Material Group Co., Ltd, Shenzhen 518107, P. R. China

[d]Department of Chemistry, KU Leuven, Celestijnenlaan 200F, Leuven 3001, Belgium. E-mail: feili.lai@kuleuven.be

[e]Institute for Condensed Matter and Nanosciences (IMCN), Bio- and Soft Matter (BSMA), Université Catholique de Louvain (UCL), Place Pasteur 1, 1348, Louvain-la-Neuve, Belgium

† Electronic supplementary information (ESI) available. See DOI: https://doi.org/10.1039/d4ta01608d

‡ These authors contributed equally to this work.

appealing alternative due to the low redox potential of K/K^+ (−2.93 V *vs.* standard hydrogen electrode) and the natural abundance of potassium resources.[12–16] Meanwhile, the APIHCs can also bring a high level of safety, environmental friendliness, and high ionic conductivity.[17–20] However, the comparatively large radius of K^+ (1.33 Å) in comparison to Li^+ (0.60 Å) has posed a significant hurdle in the development of potassium-ion storage devices, resulting from the sluggish ion transport kinetics, irreversible structure destruction, and inferior storage performance of APIHCs. Therefore, it is still necessary and challenging to develop promising electrode candidates for potassium ion storage.

Transition metal oxides (TMOs) are considered as reliable electrode candidates for APIHCs by virtue of their low cost, abundance, and superior capacity.[21–24] Among them, nickel oxide (NiO) has been extensively studied as a typical pseudocapacitive-type material due to its high theoretical capacity and exceptional charge storage properties. However, it is hampered in practical application by severe particle aggregation and low electrical conductivity, resulting in low real capacity and poor cycling lifespan. The incorporation of TMOs within reasonable carbon matrices has been demonstrated as an effective approach to solve these problems, which can endow hybrids with enhanced conductivity and structural stability.[25–27] The well-designed carbon-based substrates can prevent aggregation of active material, offer mechanical flexibility and abundant conductive pathways, and improve electrochemical storage performance.[28,29] For example, metal–organic frameworks are currently regarded as suitable precursors for creating hierarchical porous carbon nanocomposites with controllable structures. The internal voids can offer a significant number of active sites and provide short distances for ion diffusion and electrolyte penetration.[30–32] Regrettably, the conventional physical blending process of active materials and supports often results in the aggregation of individual components with poor intimate connections. This hampers the interfacial charge-transfer ability and stability severely, leading to poor rate capability.[33–35] Therefore, it is a significant challenge to establish tight interactions between electroactive materials and carbon supports that could be pivotal in storage performance. Additionally, the inherent mechanisms underlying their impact on potassium storage performance remain lacking.

Herein, we synthesized ultrathin NiO nanosheets (NSs) anchored to nitrogen-doped hierarchical porous carbon (NiO/N-HPC) and utilized it to construct an aqueous potassium-ion hybrid capacitor. The rational design endows the NiO/N-HPC hybrid with outstanding merits. (i) The hierarchical and interconnected porous architecture promotes efficient electrolyte diffusion and penetration, which can shorten ion transport path and accelerate reaction kinetics. (ii) The unique structure of the dodecahedral carbon support with a hierarchical pore structure ensures a homogeneous distribution of ultrathin NiO NSs, enhancing accessibility and exposure of active sites, and thereby promoting prolonged cycle stability. (iii) The nitrogen-doped carbon support can achieve optimized metal oxides–carbon interaction and enhance the adsorption ability for the electrolyte ions. Consequently, it was found that the resulting NiO/N-HPC showed a superior capacitance of 126.4 F g^{-1} at a current density of 0.5 A g^{-1} in 0.5 M K_2SO_4. The fabricated NiO/N-HPC//N-HPC APIHC achieved an ultra-high capacitance retention of 91.6% over 8000 cycles at the current density of 2 A g^{-1}. Meanwhile, the APIHC showed an excellent energy density of 21.95 W h kg^{-1} and a power density of 9000 W kg^{-1}.

2 Experimental sections

2.1 Materials

Zinc nitrate hexahydrate ($Zn(NO_3)_2 \cdot 6H_2O$), nickel nitrate hexahydrate ($Ni(NO_3)_2 \cdot 6H_2O$), 2-methylimidazole, ammonia, urea, methanol, ethanol, tetrahydrofuran, *N*-methyl pyrrolidone (NMP), tetrahydrofuran (THF), polyvinylidene difluoride (PVDF), carbon black, and potassium sulfate (K_2SO_4) were supplied by Sinopharm Chemical Reagent Co., Ltd. The polystyrene (PS) was prepared as reported previously.[36]

2.2 Synthesis of NiO/N-HPC

The nitrogen-doped hierarchical porous carbon (N-HPC) was prepared based on our previous work,[37] where PS microspheres were used as the template. They were soaked in 135 mL methanol solution including 20.25 g 2-methylimidazole and 24.45 g $Zn(NO_3)_2 \cdot 6H_2O$ and vacuumed for 0.5 h. Following this, the soaked PS microspheres were dried at 60 °C and then immersed in a mixed solution comprising ammonia and methanol (volumetric ratio: 1 : 2) for 24 h, resulting in the formation of single-crystal ordered macroporous zeolitic imidazolate frameworks (SOM ZIF-8). The PS template within the SOM ZIF-8 was eliminated through immersion in THF for 24 h, and then dried at 110 °C for 24 h to remove any residue. Under an Ar atmosphere, the above dried sample was carbonized at 900 °C for 1 h to yield N-HPC. Then, N-HPC (20 mg) was ultrasonicated in 34 mL of deionized water for 1 h, followed by adding urea (20 mg) and $Ni(NO_3)_2 \cdot 6H_2O$ (8 mg). After stirring for 2 h, the mixture was transferred into a 50 mL Teflon-lined autoclave and heated at 120 °C for 16 h. The obtained product, comprising $Ni(OH)_2$ nanosheets grown on the surface of N-HPC ($Ni(OH)_2$/N-HPC), was subjected to multiple centrifugation steps to remove impurities. Finally, the $Ni(OH)_2$/N-HPC composite was dried at 75 °C and then heated at 350 °C for 2 h under an Ar atmosphere to obtain ultrathin NiO nanosheets (NSs) anchored to nitrogen-doped hierarchical porous carbon (NiO/N-HPC). Furthermore, the mass ratio of NiO in the NiO/N-HPC was also detected by using thermogravimetric analysis (TGA) as shown in Fig. S1,† which is approximately 8.8 wt%.

2.3 Synthesis of bulk NiO

Urea (20 mg), $Ni(NO_3)_2 \cdot 6H_2O$ (8 mg), and 34 mL deionized water were mixed under stirring for 2 h. Then, the mixture was transferred into a 50 mL Teflon-lined autoclave and heated at 120 °C for 16 h. The sample was washed with ethanol/water and dried at 75 °C. Finally, the as-prepared samples were heated at 350 °C for 2 h under an Ar atmosphere to obtain bulk NiO.

2.4 Materials characterization

The morphologies of the samples were investigated *via* scanning electron microscopy (SEM, HITACHI S4800, Japan)

and transmission electron microscopy (TEM, JEM-2100plus, Japan). The elemental distribution on the sample was scanned by energy-dispersive X-ray spectroscopy. X-ray diffraction (XRD) patterns were recorded on an X-ray diffractometer (Bruker D8, Germany) with Cu Kα radiation ($\lambda = 1.5418$ Å). X-ray photoelectron spectroscopy (XPS, Axis Supra, British) was performed to analyze the compositions of the samples. Thermogravimetric analysis (TGA) experiments were performed with a heating rate of 10 °C min^{-1} under oxygen atmosphere using a NETZSCH STA 2500 simultaneous thermal analyzer, in the range from 30 to 1000 °C. Atomic force microscopy (AFM) measurements were performed at Bruker Dimensional Icon AFM.

2.5 Electrochemical measurements

The working electrodes were fabricated by mixing the PVDF binder, carbon black, and active material with a mass ratio of 1 : 1 : 8. The above components were prepared into a slurry with NMP and coated on carbon paper with a mass loading of about 1 mg cm^{-2}. Electrochemical measurements were conducted on a three-electrode system with a graphite electrode as the counter electrode and an Ag/AgCl electrode as the reference electrode. The cyclic voltammetry (CV) curves, galvanostatic charge–discharge (GCD) curves, and electrochemical impedance spectroscopy (EIS) plots were recorded on a CHI 660E electrochemical workstation in 0.5 M K_2SO_4 electrolyte.

The mass-based specific capacitance (C, F g^{-1}) measured on a three-electrode system was calculated from the GCD curves using the following equation:

$$C = \frac{I \times \Delta t}{m \times V} \quad (1)$$

where I (A) is the current, Δt (s) is the discharge time, m (g) is the mass of electroactive material, and V (V) is the potential.

For aqueous potassium-ion hybrid capacitors (APIHCs), they were fabricated using electrolyte (0.5 M K_2SO_4), anode (N-HPC), and cathode (NiO/N-HPC). The mass loadings of the anode and cathode were obtained by the following equation:

$$\frac{m_c}{m_a} = \frac{C_a \times \Delta V_a}{C_c \times \Delta V_c} \quad (2)$$

where m_a, C_a and ΔV_a represent the mass, specific capacitance and potential of anode, m_c, C_c and ΔV_c represent the mass, specific capacitance and potential of cathode.

The energy density (E, W h kg^{-1}) of APIHC was obtained from the following equation:

$$E = \frac{1}{2} \times C \times V^2 \quad (3)$$

The power density (P, W kg^{-1}) of APIHC was obtained from the following equation:

$$P = \frac{E}{\Delta t} \quad (4)$$

2.6 Density functional theory (DFT) calculations

DFT calculations were performed using the Vienna *ab initio* simulation package (VASP)[38,39] with the Perdew–Burke–Ernzerhof generalized gradient approximation (GGA-PBE).[40,41] It was used to describe the ion–electron interaction, employing the projected augmented wave (PAW)[42] method. A cutoff energy of 600 eV was chosen for the planewave expansion of electron wave function. A vacuum space of at least 20 Å was implemented to separate interactions between neighboring slabs. In this calculation, a 5 × 5 × 3 k-point mesh was adopted, and convergence criteria were established at 10^{-5} eV for the self-consistent field (SCF) and 10^{-2} eV $Å^{-1}$ for the ionic steps.

3 Results and discussion

The ultrathin NiO nanosheets (NSs) anchored to nitrogen-doped hierarchical porous carbon (NiO/N-HPC) nanocomposite was synthesized based on single-crystal ordered macroporous zeolitic imidazolate frameworks (SOM ZIF-8) through three steps (Fig. 1a). In particular, the hierarchical porous structure of N-HPC can be obtained by employing uniform polystyrene microspheres as the template.[43] After anchoring the $Ni(OH)_2$ NSs on the surface of N-HPC ($Ni(OH)_2$/N-HPC) through a hydrothermal process, the $Ni(OH)_2$ NSs were further transferred into NiO NSs after annealing. The scanning electron microscopy (SEM) images in Fig. 1b and c demonstrate that the N-HPC maintains the rhombic dodecahedral framework from SOM ZIF-8, while containing abundant and uniform pores with uniform distributions of C, O, and N elements (Fig. S2†). Fig. 1d and e reveal that the ultrathin NiO NSs are uniformly grown on the surface of the dodecahedral carbon support. The transmission electron microscopy (TEM) image of NiO/N-HPC (Fig. 1f) further confirms its hierarchical porous structure with tightly anchored ultrathin NiO NSs. The atomic force microscopy (AFM) image (Fig. S3†) indicates that the thickness of the ultrathin NiO NSs in NiO/N-HPC hybrids is only about 1.97 nm. Apparently, this ultrathin structural feature can effectively contribute to the high specific surface area and abundant active sites. Importantly, the tight integration of the NiO NSs to the surface of N-HPC is favorable for fast electron transfer between these two heterogeneous components. In contrast, the irregular bulk of NiO NSs prepared without the N-HPC substrate exhibits obvious agglomeration (Fig. S4†). The high-resolution TEM (HRTEM) image of NiO/N-HPC (Fig. 1g) shows that the lattice plane distances for NiO/N-HPC are about 0.24 and 0.21 nm, which can be attributed to the (101) and (012) planes of the NiO phase, respectively.[44]

The X-ray diffraction (XRD) patterns of NiO/N-HPC, $Ni(OH)_2$/N-HPC, bulk NiO, and N-HPC are depicted in Fig. 2a. The broad and weak peaks located at 24° belong to the (002) planes of the carbon phases in NiO/N-HPC, $Ni(OH)_2$/N-HPC, and N-HPC. The diffraction peaks in $Ni(OH)_2$/N-HPC at 11.3°, 22.7°, 34.4°, and 59.9° can be attributed to the (003), (006), (012), and (110) planes of the $Ni(OH)_2$ phase (JCPDS card no. 38-0715), confirming the preparation of $Ni(OH)_2$ NSs on the N-HPC. After the annealing treatment under Ar atmosphere, three characteristic

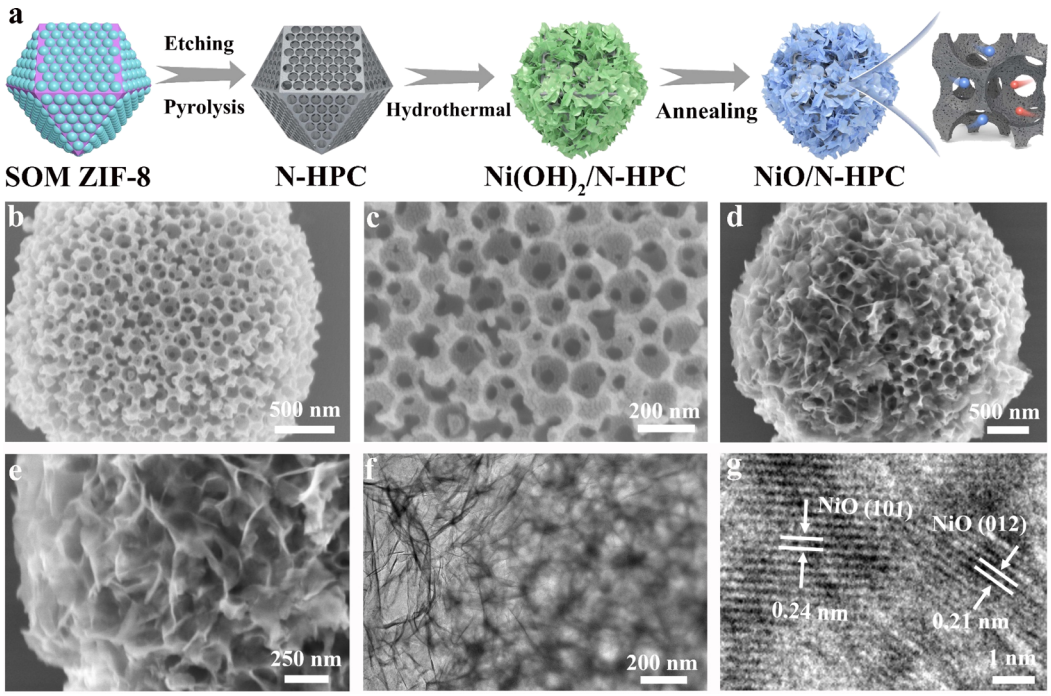

Fig. 1 (a) Schematic illustration for the synthesis of the NiO/N-HPC composite. (b and c) SEM images of N-HPC with different magnifications. (d and e) SEM images of NiO/N-HPC with different magnifications. (f) TEM and (g) HRTEM images of NiO/N-HPC.

peaks of NiO/N-HPC appear at 37.3°, 43.3°, and 62.8°, which can be assigned to the (101), (012), and (110) planes of the NiO phase.[45] Furthermore, X-ray photoelectron spectroscopy (XPS) was conducted to analyze the elemental composition and valence state of NiO/N-HPC. In the high-resolution Ni 2p XPS spectrum of NiO/N-HPC (Fig. 2b), there are two prominent peaks at about 855.7 and 873.5 eV, which can be assigned to Ni $2p_{3/2}$ and Ni $2p_{1/2}$, respectively.[46] After fitting the high-

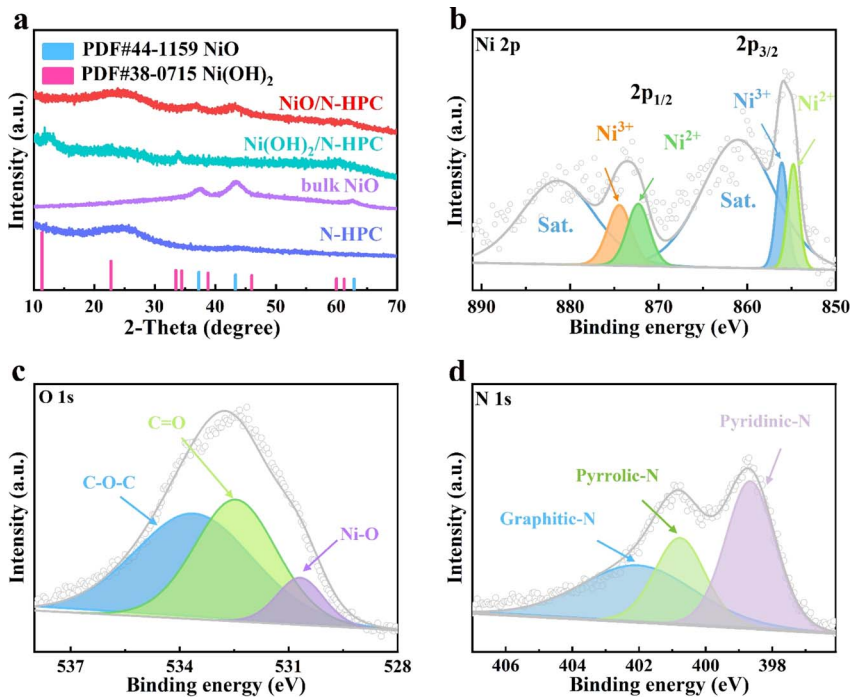

Fig. 2 (a) XRD patterns of NiO/N-HPC, $Ni(OH)_2$/N-HPC, bulk NiO, and N-HPC. High-resolution XPS spectra for (b) Ni 2p, (c) O 1s, and (d) N 1s of NiO/N-HPC.

resolution O 1s XPS spectrum of NiO/N-HPC in Fig. 2c, there are three peaks at 530.7, 532.5, and 533.6 eV, attributed to the Ni–O, C═O, and C–O–C species, respectively. In the high-resolution N 1s spectrum of NiO/N-HPC shown in Fig. 2d, three peaks represent the existences of pyridinic-N, pyrrolic-N, and graphitic-N.[47,48] The nitrogen doping strategy can enhance the electrolyte wettability and the electrical conductivity of NiO/N-HPC.[49]

The potassium-ion storage performance of NiO/N-HPC, $Ni(OH)_2$/N-HPC, and bulk NiO was measured within the voltage window of 0–0.9 V in 0.5 M K_2SO_4 electrolyte. Fig. 3a shows the cyclic voltammetry (CV) curves of NiO/N-HPC, $Ni(OH)_2$/N-HPC, and bulk NiO at the scan rate of 100 mV s^{-1}. The CV curves of NiO/N-HPC exhibit nearly rectangular shapes within the voltage range between 0 and 0.9 V, indicating their characteristic double-layer capacitance behavior. As the galvanostatic charge–discharge (GCD) curves at the current density of 1 A g^{-1} shown in Fig. 3b, the specific capacitances of NiO/N-HPC, $Ni(OH)_2$/N-HPC, and bulk NiO are 112.0, 88.3, and 39.1 F g^{-1}, respectively. The GCD curves of NiO/N-HPC show classical triangular shapes with linear-like voltage–time relationships at different current densities ranging from 0.5 to 10 A g^{-1},

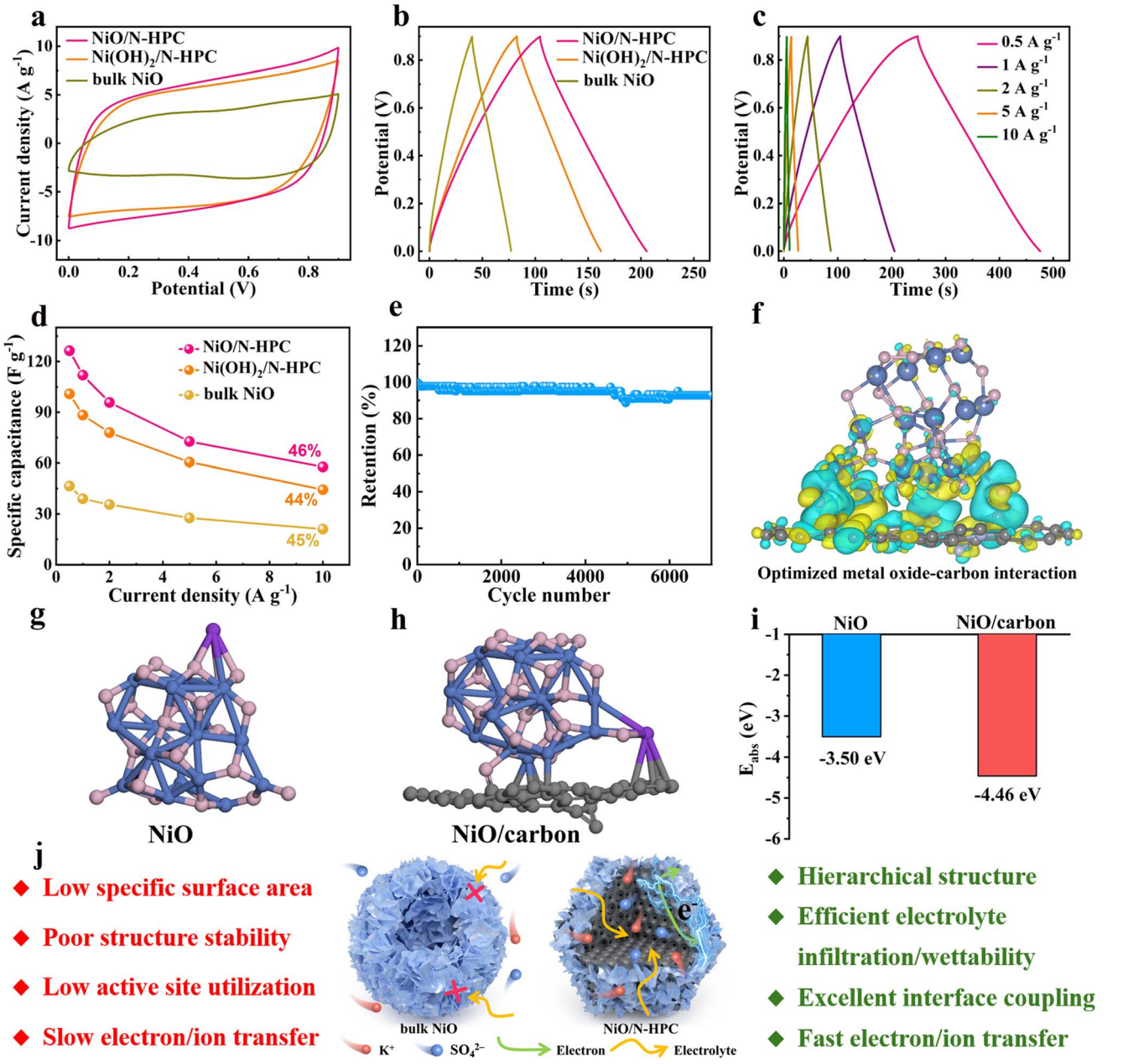

Fig. 3 (a) CV curves at the scan rate of 100 mV s^{-1} and (b) GCD curves at 1 A g^{-1} for NiO/N-HPC, $Ni(OH)_2$/N-HPC, and bulk NiO. (c) GCD curves under various current densities of NiO/N-HPC. (d) Specific capacitance under various current densities. (e) Cycling performance of NiO/N-HPC. (f) The difference charge density of NiO/carbon. The atomic models of potassium adsorption in (g) NiO and (h) NiO/carbon. (i) The adsorption energy of potassium ion in NiO and NiO/carbon. (j) Schematic illustration of the merits of NiO/N-HPC compared with bulk NiO.

further demonstrating the typical double-layer capacitance behavior of NiO/N-HPC. The highest specific capacitance of NiO/N-HPC can even reach 126.4 F g^{-1} at a low current density of 0.5 A g^{-1} (Fig. 3c). As shown in Fig. 3d, the NiO/N-HPC achieves higher specific capacitance values at various current densities than those of $Ni(OH)_2$/N-HPC, bulk NiO, and N-HPC. The NiO/N-HPC also shows a higher capacitance retention of 46%. Moreover, the NiO/N-HPC exhibits an ultrahigh capacitance retention of 92.8% after 7000 cycles (Fig. 3e), which demonstrates its excellent long-cycling stability. Meanwhile, the similarity in chemical composition and valence state of NiO/N-HPC before and after cycling processes, underscores the good stability of the NiO/N-HPC throughout the cycling process (Fig. S6†).

Density functional theory (DFT) calculations were further employed to investigate the impact of interfacial engineering on potassium storage performance. As shown in Fig. 3f, the well-connected interface between NiO and carbon support promotes charge delocalization between NiO and carbon support, facilitating accelerated electron transfer and consequent enhancement in electrical conductivity compared to bulk NiO. Upon optimizing the structural configuration of NiO and NiO/carbon with adsorbed K^+ ion (Fig. 3g and h), the adsorption energy (E_{ads}) values are −3.50 and −4.46 eV for NiO and NiO/carbon (Fig. 3i), respectively. This result suggests that the improved metal oxides-carbon interactions between NiO and carbon support contribute to the enhanced K ions storage. Based on the above electrochemical analysis and simulation, the superior potassium storage performance of NiO/N-HPC can be summarized in the following advantages (Fig. 3j). (i) The dodecahedral carbon support facilitates a homogeneous distribution of ultrathin NiO NSs to enhance the accessibility of the fully exposed active sites and promote prolonged cycle stability. (ii) The hierarchical and interconnected architecture of NiO/N-HPC enables efficient penetration and diffusion of the electrolyte during the electrochemical process, reducing the

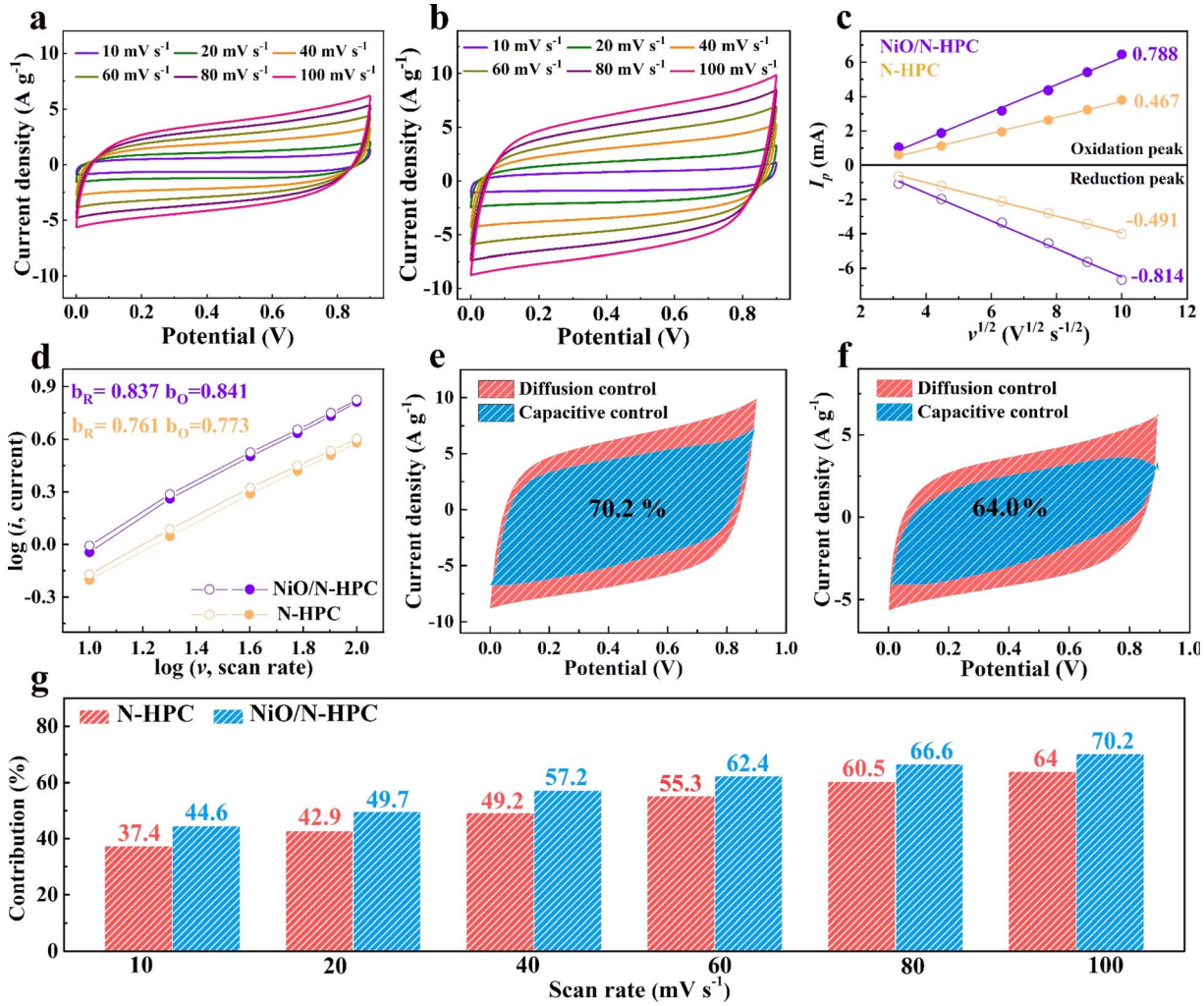

Fig. 4 The CV curves at different scan rates for (a) N-HPC and (b) NiO/N-HPC. (c) The linear relation between I_p and $v^{1/2}$, and (d) the relation between log(*i*) and log(*v*) of N-HPC and NiO/N-HPC (hollow: reduction peak; solid: oxidation peak). (e and f) The contribution of the capacitance (blue) and the diffusion (red) in the CV profiles of NiO/N-HPC and N-HPC at a scan rate of 100 mV s^{-1}. (g) Normalized proportions for capacitance contributions of N-HPC and NiO/N-HPC.

interface impedance and shortening ion transport paths. (iii) The nitrogen-doped carbon support can achieve optimized metal oxides–carbon interaction and enhance the adsorption ability for the electrolyte ions.

The storage kinetics behavior of NiO/N-HPC and N-HPC was further investigated by CV measurement at various scan rates from 10 to 100 mV s^{-1}. As shown in Fig. 4a and b, the NiO/N-HPC shows larger CV areas than those of the N-HPC under the same scan rates, implying its enhanced capacitive performance. In addition, Fig. 4c reveals the linear relationships between I_p and $v^{1/2}$ of NiO/N-HPC and N-HPC. The slope values for NiO/N-HPC are 0.788 (oxidation peak) and −0.814 (reduction peak), which are higher than those for N-HPC (0.467 and −0.491), indicating the improved ion transfer capability of NiO/N-HPC due to its hierarchical porous structure.[50] The correlation between the logarithm peak current and the scan rate was further calculated (based on the equation of $I = a^v b$, where a and b are variable constants) to distinguish between diffusion- or capacitive-control processes. As shown in Fig. 4d, the slope values (calculated b-value) of NiO/N-HPC (0.837 and 0.841) are higher than those of N-HPC (0.761 and 0.773), proving the enhanced capacitive potassium-ion storage of NiO/N-HPC. Specifically, the contribution ratios of capacitive- and diffusion- controls were further determined using formulae ($i = k_1v + k_2v^{1/2}$ and $i/v^{1/2} = k_1v^{1/2} + k_2$). The NiO/N-HPC shows a higher capacitive contribution ratio of 70.2% at the scan rate of 100 mV s^{-1} compared to 64.0% for N-HPC (Fig. 4e and f). By increasing the scan rate, the capacitive contribution of NiO/N-HPC increases gradually and remains higher than that of N-HPC at the same scan rate (Fig. 4g). These results indicate that more ions can adsorb onto the surface of NiO/N-HPC compared to N-HPC during the high-rate charging/discharging process,

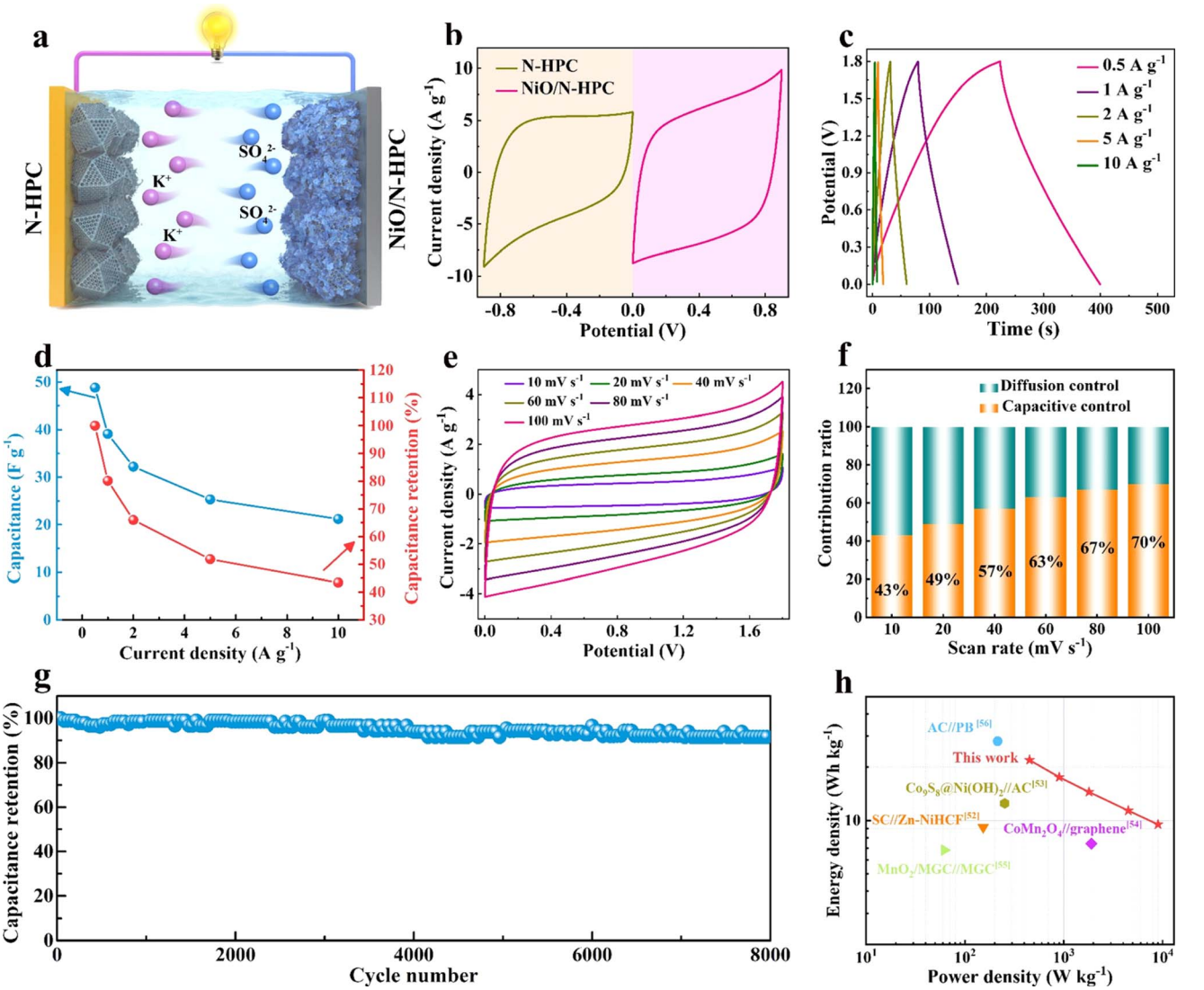

Fig. 5 (a) Schematic illustration of NiO/N-HPC//N-HPC APIHCs. (b) CV curves of the NiO/N-HPC cathode and N-HPC anode at a scan rate of 100 mV s^{-1}. (c) GCD profiles, (d) specific capacitance and the corresponding capacitance retention of APIHCs under different current densities. (e) CV curves and (f) corresponding capacitive contributions of APIHCs at different scan rates. (g) Cycling performance of APIHCs. (h) Ragone plots of APIHCs compared with previously reported energy storage devices.

followed by a dominant capacitance-controlled electrochemical behavior.[51] The homogeneously distributed NiO NSs and hierarchical porous channels in NiO/N-HPC confer a more exposed surface area, leading to abundant active boundaries that favor capacitive-control electrochemical behavior.

To further evaluate the practical application of NiO/N-HPC in the aqueous potassium-ion hybrid capacitors (APIHCs), NiO/N-HPC//N-HPC APIHCs were assembled by employing N-HPC as the anode and NiO/N-HPC as the cathode (Fig. 5a). As shown in Fig. 5b, the CV curves of the NiO/N-HPC cathode and N-HPC anode were tested at 100 mV s^{-1} in an aqueous K_2SO_4 electrolyte. By balancing the total charge of the two electrodes, $Q^+ \times m^+ = Q^- \times m^-$, the mass loading of the electrode was continuously adjusted to achieve optimal storage performance. Meanwhile, with the combination of the NiO/N-HPC cathode (0 to 0.9 V) and N-HPC anode (−0.9 to 0 V), the operating voltage of the APIHC can be further increased to 1.8 V. Fig. 5c displays the GCD curves of the NiO/N-HPC//N-HPC APIHCs with symmetrical shapes, demonstrating their typical capacitive behavior and high degrees of reversibility. The specific capacitances of the NiO/N-HPC//N-HPC APIHCs (Fig. 5d) calculated from the GCD curves are 48.8, 39.1, 32.2, 25.3, and 21.1 F g^{-1} at current densities of 0.5, 1, 2, 5, and 10 A g^{-1}, respectively. The NiO/N-HPC//N-HPC APIHC maintains the typical rectangular CV curves as the scan rate increases from 10 to 100 mV s^{-1} (Fig. 5e) and exhibits a high capacitive contribution ratio of 70% at 100 mV s^{-1} (Fig. 5f), indicating its excellent capacitive behavior. More importantly, the NiO/N-HPC//N-HPC APIHC achieves ultra-high capacitance retention of 91.6% over 8000 cycles at the current density of 2 A g^{-1} (Fig. 5g), implying its superior cycling stability. The NiO/N-HPC//N-HPC APIHC shows a maximal energy density of 21.95 W h kg^{-1} and a maximal power density of 9000 W kg^{-1} (Fig. 5h), which is superior to those of most previously reported capacitors, such as SC//Zn–NiHCF,[52] Co_9S_8@$Ni(OH)_2$//AC,[53] $CoMn_2O_4$//graphene,[54] MnO_2/MGC//MGC,[55] and AC//PB[56] (Table S1†).

4 Conclusion

In summary, a nanocomposite consisting of ultrathin NiO nanosheets (NSs) anchored to nitrogen-doped hierarchical porous carbon (NiO/N-HPC) was rationally designed and applied to construct an aqueous potassium-ion hybrid capacitor. The unique structure of the dodecahedral carbon support with abundant pores achieves homogeneous distribution of ultrathin NiO NSs, promoting accessibility and exposure of active sites and excellent cycling stability. The hierarchical and interconnected architecture of the NiO/N-HPC promotes efficient electrolyte penetration and diffusion, shortens ion transport channels and accelerates reaction kinetics. Moreover, excellent metal oxides–carbon interactions can be constructed by introducing nitrogen doping on the carbon surface, leading to an interfacial coupling effect between NiO and N-HPC for boosted electron/ion transfer. Therefore, the NiO/N-HPC shows an enhanced capacitance of 126.4 F g^{-1} at a current density of 0.5 A g^{-1} in 0.5 M K_2SO_4. Furthermore, the as-fabricated NiO/N-HPC//N-HPC APIHC achieved ultra-high capacitance retention of 91.6% over 8000 cycles at the current density of 2 A g^{-1}. Meanwhile, the NiO/N-HPC//N-HPC APIHC shows an excellent energy density of 21.95 W h kg^{-1} and a power density of 9000 W kg^{-1}. This study offers an attractive avenue to design TMOs/carbon hybrids with hierarchical architectures for high-performance aqueous potassium-ion hybrid capacitors.

Data availability

The data supporting this article have been included in Figures and Tables, as well as a part of the ESI.†

Author contributions

Tianlu Wang: conceptualization, investigation, resources, writing – original draft, writing – review & editing. Wei Zong: conceptualization, investigation, writing – original draft, writing – review & editing. Jieru Yang: conceptualization, investigation, writing – review & editing. Leiqian Zhang, Jian Meng, Jiale Ge, Guozheng Yang, Jianguo Ren, Peng He, Elke Debroye, and Jean-François Gohy: formal analysis, writing – review & editing. Feili Lai: supervision, writing – review & editing. Tianxi Liu: supervision, writing – review & editing. All authors analyzed the data, discussed the results and commented on the manuscript.

Conflicts of interest

The authors declare no conflicts of interest.

Acknowledgements

This work was supported by the National Natural Science Foundation of China (52303342), the Research Foundation-Flanders (FWO, Grant No. 1298323N and V404923N), and the research on the industrial application of "controllable synthesis of nanocarbon-based polymer composites and their application in new energy" (CJGJZD20210408092400002). F.L. acknowledges the "Xiaomi Young Scholars" program. E.D. acknowledges funding by the KU Leuven Internal Funds (Grant Numbers C14/23/090 and CELSA/23/018), and the European Union (ERC Starting Grant, 101117274 X-PECT). Views and opinions expressed are however those of the authors only and do not necessarily reflect those of the European Union or European Research Council. Neither the European Union nor the granting authority can be held responsible for them. We also thank the characterizations supported by the Central Laboratory, School of Chemical and Material Engineering, Jiangnan University.

References

1 B. Dunn, H. Kamath and J.-M. Tarascon, *Science*, 2011, **334**, 928–935.
2 C. Zhu, J. Wu, J. Yan and X. Liu, *Adv. Fiber Mater.*, 2022, **5**, 12–35.

3 Z.-X. Huang, X.-L. Zhang, X.-X. Zhao, Y.-L. Heng, T. Wang, H. Geng and X.-L. Wu, *Sci. China Mater.*, 2023, **66**, 79–87.
4 Y. Ouyang, X. Li, J. Zhu, W. Zong, Y. Dai, X. Gao, W. Zhang, S. Yang, R. Bagherzadeh, F. Lai, Y.-E. Miao and T. Liu, *Nano Res.*, 2024, **17**, 1473–1481.
5 Y. Cheng, L. Yang and S. Yin, *Compos. Commun.*, 2023, **40**, 101588.
6 Z. Li, S. Gadipelli, H. Li, C. A. Howard, D. J. L. Brett, P. R. Shearing, Z. Guo, I. P. Parkin and F. Li, *Nat. Energy*, 2020, **5**, 160–168.
7 Y. Dai, C. Zhang, J. Li, X. Gao, P. Hu, C. Ye, H. He, J. Zhu, W. Zhang, R. Chen, W. Zong, F. Guo, I. P. Parkin, D. J. L. Brett, P. R. Shearing, L. Mai and G. He, *Adv. Mater.*, 2024, **36**, 2310645.
8 Y. Gogotsi and P. Simon, *Science*, 2011, **334**, 917–918.
9 C. Xu, X. Yang, C. Hu, J. Zhang, L. Yang and S. Yin, *Compos. Commun.*, 2024, **45**, 101814.
10 F. Lai, J. Feng, T. Hei, G.-C. Wang, P. Adler, M. Antonietti and M. Oschatz, *Energy Storage Mater.*, 2019, **20**, 188–195.
11 W. Zhang, Y. Dai, R. Chen, Z. Xu, J. Li, W. Zong, H. Li, Z. Li, Z. Zhang, J. Zhu, F. Guo, X. Gao, Z. Du, J. Chen, T. Wang, G. He and I. Parkin, *Angew. Chem., Int. Ed.*, 2023, **62**, e202212695.
12 X. Zhang, T. Xiong, B. He, S. Feng, X. Wang, L. Wei and L. Mai, *Energy Environ. Sci.*, 2022, **15**, 3750–3774.
13 Y. Lou, P. Li, H. He, S. Zhou, Y. Cai, B. Chen and M. Zhang, *Sci. China Mater.*, 2023, **66**, 3093–3103.
14 M. Huang, X. Wang, J. Meng, X. Liu, X. Yao, Z. Liu and L. Mai, *Nano Energy*, 2020, **77**, 105069.
15 W. Zong, N. Chui, Z. Tian, Y. Li, C. Yang, D. Rao, W. Wang, J. Huang, J. Wang, F. Lai and T. Liu, *Adv. Sci.*, 2021, **8**, 2004142.
16 C. Yang, J. Feng, F. Lv, J. Zhou, C. Lin, K. Wang, Y. Zhang, Y. Yang, W. Wang, J. Li and S. Guo, *Adv. Mater.*, 2018, **30**, 1800036.
17 J.-Y. Luo, W.-J. Cui, P. He and Y.-Y. Xia, *Nat. Chem.*, 2010, **2**, 760–765.
18 W. Zhong, C. Zhang, S. Li, W. Zhang, Z. Zeng, S. Cheng and J. Xie, *Sci. China Mater.*, 2023, **66**, 903–912.
19 Z. Liu, Y. Huang, Y. Huang, Q. Yang, X. Li, Z. Huang and C. Zhi, *Chem. Soc. Rev.*, 2020, **49**, 180–232.
20 Q. Chen, J. Jin, M. Song, X. Zhang, H. Li, J. Zhang, G. Hou, Y. Tang, L. Mai and L. Zhou, *Adv. Mater.*, 2022, **34**, 2107992.
21 S. K. Hussain, G. Nagaraju, S. C. Sekhar and J. S. Yu, *Energy Storage Mater.*, 2020, **27**, 405–417.
22 N. Ali, T. Hussain, X. Wang, J. Yu and B. Ding, *Compos. Commun.*, 2023, **40**, 101604.
23 D. K. Pathak, T. Ghosh and R. Kumar, *J. Energy Storage*, 2023, **67**, 107643.
24 J. Li, N. Luo, L. Kang, F. Zhao, Y. Jiao, T. J. Macdonald, M. Wang, I. P. Parkin, P. R. Shearing, D. J. L. Brett, G. Chai and G. He, *Adv. Energy Mater.*, 2022, **12**, 2201840.
25 P. Chen, N. Zhang, S. Wang, T. Zhou, Y. Tong, C. Ao, W. Yan, L. Zhang, W. Chu, C. Wu and Y. Xie, *Proc. Natl. Acad. Sci. U. S. A.*, 2019, **116**, 6635–6640.
26 W. Zong, H. Gao, Y. Ouyang, K. Chu, H. Guo, L. Zhang, W. Zhang, R. Chen, Y. Dai, F. Guo, J. Zhu, Z. Zhang, C. Ye, Y.-E. Miao, J. Hofkens, F. Lai and T. Liu, *Angew. Chem., Int. Ed.*, 2023, **62**, e202218122.
27 P. Ge, S. Li, L. Xu, K. Zou, X. Gao, X. Cao, G. Zou, H. Hou and X. Ji, *Adv. Energy Mater.*, 2019, **9**, 1803035.
28 R. Yan, K. Leus, J. P. Hofmann, M. Antonietti and M. Oschatz, *Nano Energy*, 2020, **67**, 104240.
29 J. Zhang, Z. Xia and L. Dai, *Sci. Adv.*, 2015, **1**, e1500564.
30 S. Chen, W.-H. Li, W. Jiang, J. Yang, J. Zhu, L. Wang, H. Ou, Z. Zhuang, M. Chen, X. Sun, D. Wang and Y. Li, *Angew. Chem., Int. Ed.*, 2022, **61**, e202114450.
31 G. Cai, P. Yan, L. Zhang, H.-C. Zhou and H.-L. Jiang, *Chem. Rev.*, 2021, **121**, 12278–12326.
32 Z. Ye, Y. Jiang, L. Li, F. Wu and R. Chen, *eScience*, 2023, **3**, 100107.
33 W. Zong, H. Guo, Y. Ouyang, L. Mo, C. Zhou, G. Chao, J. Hofkens, Y. Xu, W. Wang, Y.-E. Miao, G. He, I. P. Parkin, F. Lai and T. Liu, *Adv. Funct. Mater.*, 2022, **32**, 2110016.
34 H. Jin, S. Xin, C. Chuang, W. Li, H. Wang, J. Zhu, H. Xie, T. Zhang, Y. Wan, Z. Qi, W. Yan, Y. R. Lu, T. S. Chan, X. Wu, J. B. Goodenough, H. Ji and X. Duan, *Science*, 2020, **370**, 192–197.
35 P. Chen, K. Xu, T. Zhou, Y. Tong, J. Wu, H. Cheng, X. Lu, H. Ding, C. Wu and Y. Xie, *Angew. Chem., Int. Ed.*, 2016, **55**, 2488–2492.
36 F. Gao, J. Qu, C. Geng, G. Shao and M. Wu, *J. Mater. Chem. A*, 2016, **4**, 7445–7452.
37 J. Yang, J. Meng, L. Zhang, K. Chu, W. Zong, L. Ge, S. Fu, J. Ge, H. Zhu, G. He, D. J. L. Brett, F. Lai and T. Liu, *J. Power Sources*, 2022, **549**, 232111.
38 G. Kresse and J. Furthmüller, *Phys. Rev. B: Condens. Matter Mater. Phys.*, 1996, **54**, 11169–11186.
39 G. Kresse and J. Hafner, *Phys. Rev. B: Condens. Matter Mater. Phys.*, 1993, **48**, 13115–13118.
40 G. Kresse and J. Furthmüller, *Comput. Mater. Sci.*, 1996, **6**, 15–50.
41 J. P. Perdew, K. Burke and M. Ernzerhof, *Phys. Rev. Lett.*, 1996, **77**, 3865–3868.
42 P. E. Blochl, *Phys. Rev. B: Condens. Matter Mater. Phys.*, 1994, **50**, 17953–17979.
43 H. Hong, J. Liu, H. Huang, C. A. Etogo, X. Yang, B. Guan and L. Zhang, *J. Am. Chem. Soc.*, 2019, **141**, 14764–14771.
44 R. Ahmed and G. Nabi, *J. Energy Storage*, 2021, **33**, 102115.
45 J. Zhang, W. Luo, T. Xiong, R. Yu, P. Wu, J. Zhu, Y. Dai and L. Mai, *Nanoscale*, 2019, **11**, 7588–7594.
46 W. Jae, J. Song, J. J. Hong and J. Kim, *J. Alloys Compd.*, 2019, **805**, 957–966.
47 W. Zong, F. Lai, G. He, J. Feng, W. Wang, R. Lian, Y. E. Miao, G. C. Wang, I. P. Parkin and T. Liu, *Small*, 2018, **14**, 1801562.
48 F. Zhang, S. Ji, H. Wang, H. Liang, X. Wang and R. Wang, *Small Methods*, 2021, **5**, 2100066.
49 L. Wan, E. Shamsaei, C. D. Easton, D. Yu, Y. Liang, X. Chen, Z. Abbasi, A. Akbari, X. Zhang and H. Wang, *Carbon*, 2017, **121**, 330–336.
50 V. Augustyn, J. Come, M. A. Lowe, J. W. Kim, P.-L. Taberna, S. H. Tolbert, H. D. Abruna, P. Simon and B. Dunn, *Nat. Mater.*, 2013, **12**, 518–522.

51 T. Brezesinski, J. Wang, S. H. Tolbert and B. Dunn, *Nat. Mater.*, 2010, **9**, 146–151.
52 D. Ramon Lobato-Peralta, J. Vazquez-Samperio, O. Perez, P. Acevedo-Pena, E. Reguera and A. Karina Cuentas-Gallegos, *J. Energy Storage*, 2020, **31**, 101667.
53 F. Zhu, M. Yan, Y. Liu, H. Shen, Y. Lei and W. Shi, *J. Mater. Chem. A*, 2017, **5**, 22782–22789.
54 P. Ahuja, V. Sahu, S. K. Ujjain, R. K. Sharma and G. Singh, *Electrochim. Acta*, 2014, **146**, 429–436.
55 Y. He, W. Chen, X. Li, Z. Zhang, J. Fu, C. Zhao and E. Xie, *ACS Nano*, 2013, **7**, 174–182.
56 L. Zhou, M. Zhang, Y. Wang, Y. Zhu, L. Fu, X. Liu, Y. Wu and W. Huang, *Electrochim. Acta*, 2017, **232**, 106–113.

